

Quantum Approximate Optimization Algorithm with Cat Qubits

Pontus Vikstål,^{1,*} Laura García-Álvarez,¹ Shruti Puri,^{2,3} and Giulia Ferrini¹

¹*Wallenberg Centre for Quantum Technology, Department of Microtechnology and Nanoscience, Chalmers University of Technology, 412 96 Gothenburg, Sweden*

²*Department of Applied Physics, Yale University, New Haven, Connecticut 06511, USA*

³*Yale Quantum Institute, Yale University, New Haven, Connecticut 06511, USA*

(Dated: September 18, 2024)

The Quantum Approximate Optimization Algorithm (QAOA)—one of the leading algorithms for applications on intermediate-scale quantum processors—is designed to provide approximate solutions to combinatorial optimization problems with shallow quantum circuits. Here, we study QAOA implementations with cat qubits, using coherent states with opposite amplitudes. The dominant noise mechanism, i.e., photon losses, results in Z -biased noise with this encoding. We consider in particular an implementation with Kerr resonators. We numerically simulate solving MaxCut problems using QAOA with cat qubits by simulating the required gates sequence acting on the Kerr non-linear resonators, and compare to the case of standard qubits, encoded in ideal two-level systems, in the presence of single-photon loss. Our results show that running QAOA with cat qubits increases the approximation ratio for random instances of MaxCut with respect to qubits encoded into two-level systems.

I. INTRODUCTION

Variational quantum algorithms [1, 2], combining quantum and classical computation in a hybrid approach, occupy a central role in current research on quantum algorithms. These algorithms are promising for implementations on NISQ devices [3], since they can in principle run on shallow quantum processors. In particular, the Quantum Approximate Optimization Algorithm (QAOA) [4] can be used to tackle combinatorial optimization problems, which are omnipresent in logistics, with applications within the automotive sector [5, 6], or aviation, e.g., aircraft [7] or gate [8] assignment, financial portfolio optimization [9], among others. First proof-of-principle implementations of QAOA in superconducting qubit devices were used to solve MaxCut [10, 11] and Exact Cover [12, 13] problems. Although the performance of QAOA improves at increasing algorithmic depth provided optimal parameters, current NISQ hardware is limited by noise, which decreases the performance of QAOA after a certain algorithmic depth [11]. As such, research into different avenues for hardware implementations of QAOA that could allow for reaching deeper circuits is needed.

In this work, we explore the implementation of QAOA in bosonic systems. These have led to promising quantum computing implementations in a variety of physical settings including optical [14] and microwave radiation [15–17], trapped ions [18–20], opto-mechanical systems [21–23], atomic ensembles [24–27], and hybrid systems [28]. For example, in the microwave regime, bosonic codes have successfully extended the life-time of quantum information in superconducting cavities compared to the system’s constituents [29–31].

So far, bosonic implementations of QAOA have primarily focused on optimizing continuous functions defined on real numbers [32, 33], with little attempt made to address QAOA for solving discrete optimization problems in the context of bosonic systems, which is the focus of our work.

Encoding qubits into the coherent states of cavities fields $|\pm\alpha\rangle$, yielding cat qubits, is an emerging approach that results in biased noise. Such type of noise affects a quantum system in a non-uniform way, i.e., certain types of errors are more likely to occur than others. This encoding can thus lead to favorable error-correcting properties [34, 35], and to enhanced algorithmic performance [36].

In a previous work [37], some of the authors have shown that biased-noise qubits also allow for implementing error mitigation techniques and achieving higher performance ratios in QAOA compared to standard qubits. However, those results were obtained for a generic noise-biased error model, without considering specific implementations. In this work, we explore QAOA using cat qubits, achieved in particular by means of the driven Kerr non-linear resonator [38]. First, we simulate solving a two-qubit Exact Cover problem under the full master equation with cat qubits as a proof of principle demonstration. Second, to simulate larger cat qubit systems, we use the Pauli-transfer matrix formalism to characterize the error channel induced by single-photon losses on the computational subspace. We numerically show that for 6, 8 and 10-qubit MaxCut problems the use of cat qubits yields an improvement of the algorithmic approximation ratio with respect to the case of qubits encoded into discrete two-level systems, given equal average gate fidelities between the two systems. While we are going to focus on driven Kerr-nonlinear resonator, the implementation of QAOA on cat qubits yielding enhanced algorithmic performance unveiled in our work could also be achieved by means of other platforms, both in the superconducting [39], as well

* e-mail: vikstal@chalmers.se

as photonics [40], or other bosonic systems [41].

The paper is structured as follows. In [Section II](#) we recall the definition of cat qubits as well as the gates needed to operate them. In [Section III](#) we outline how QAOA can be run on cat qubits. We first show the principle by considering a two-qubit toy model for solving the Exact Cover problem, and then consider more extensive simulations up to 8 qubits for solving MaxCut, in the presence of photon losses. We then compare the performance of QAOA with cat qubits to the one with standard qubits given the same average gate fidelity of the two systems. We provide our conclusive remarks in [Section IV](#). In [Appendix A](#) we recall the definition of quantum gates acting on cat qubits. In [Appendix B](#) we provide some details regarding the numerical optimization. Finally, in [Appendix C](#) we introduce a bosonic version of QAOA by Trotterizing the relevant quantum annealing Hamiltonian, and we compare its performance to QAOA for the case of a single Ising spin.

II. CAT QUBITS AND HOW TO OPERATE ON THEM

In this section we recall the main properties of cat qubits implemented by means of the Kerr nonlinear resonator (KNR) as introduced in Refs. [42, 43], and summarize how to perform gates on such a cat qubit, aiming at providing a self-consistent introduction.

A. The Kerr nonlinear resonator

The cat qubit can be realized in a Kerr parametric oscillator with a two-photon pump [39, 42–44]. In a frame rotating at the frequency of the two-photon pump and in the rotating-wave approximation, the Hamiltonian for a KNR is given by (we use $\hbar = 1$ throughout this paper)

$$\hat{H}_1 = -\Delta \hat{a}^\dagger \hat{a} - K \hat{a}^{\dagger 2} \hat{a}^2 + G(\hat{a}^{\dagger 2} e^{i2\phi} + \hat{a}^2 e^{-i2\phi}), \quad (1)$$

where $\Delta = \omega_r - 2\omega_p$ is the detuning of the resonator frequency from twice the two-photon pump frequency, K is the amplitude of the Kerr non-linearity, G and ϕ are the amplitude and phase of the two-photon drive respectively. We assume that K is a nonzero positive constant and that Δ is non-negative. When the detuning is zero (i.e. when the two-photon drive frequency is half the resonator frequency) and when the phase ϕ is zero, the KNR Hamiltonian can be written as

$$\begin{aligned} \hat{H}_1 &= -K \hat{a}^{\dagger 2} \hat{a}^2 + G(\hat{a}^{\dagger 2} + \hat{a}^2) \\ &= -K \left(\hat{a}^{\dagger 2} - \frac{G}{K} \right) \left(\hat{a}^2 - \frac{G}{K} \right) + \frac{G^2}{K}. \end{aligned} \quad (2)$$

Since $\hat{a}|\alpha\rangle = \alpha|\alpha\rangle$, the coherent states $|\pm\alpha\rangle$ with $\alpha = \sqrt{G/K}$ are degenerate eigenstates of the Hamiltonian in Eq. (2) with eigenenergy G^2/K . The combinations of

these degenerate eigenstates given by $|C_\alpha^\pm\rangle = N_\pm(|\alpha\rangle \pm |-\alpha\rangle)$ with $N_\pm = \sqrt{2(1 \pm e^{-2|\alpha|^2})}$ are the so-called cat states. These states are also degenerate eigenstates and have a well defined even and odd parity, with the parity operator $\hat{\Pi} = e^{i\pi \hat{a}^\dagger \hat{a}}$.

We can take advantage of this well-defined subspace to encode our computational basis states $|\bar{0}\rangle, |\bar{1}\rangle$, defining the qubit (the bar notation is used to distinguish the computational states from the zero and one photon Fock state). To this aim, one possibility is to directly identify the qubit basis states with $|\alpha\rangle$ and $|-\alpha\rangle$ [38]. However, these states are quasi-orthogonal as $\langle -\alpha|\alpha\rangle = e^{-2\alpha^2}$, and only become orthogonal in the high photon number limit. Another possibility consists in choosing the following encoding [45]:

$$|\bar{0}\rangle = \frac{|C_\alpha^+\rangle + |C_\alpha^-\rangle}{\sqrt{2}}, \quad |\bar{1}\rangle = \frac{|C_\alpha^+\rangle - |C_\alpha^-\rangle}{\sqrt{2}}. \quad (3)$$

In this case, the computational basis states are orthogonal even for small α , while for large α they are approximately equal to $|\bar{0}\rangle \approx |\alpha\rangle$ and $|\bar{1}\rangle \approx |-\alpha\rangle$. For single-photon losses, the encoding of Eq. (3) constitutes a noise-biased qubit where the loss of a single-photon results in a phase error plus an exponentially small bit-flip error on the computational states with respect to α . Indeed, by defining the projection operator $\hat{I} = |\bar{0}\rangle\langle\bar{0}| + |\bar{1}\rangle\langle\bar{1}|$, its action on the annihilation operator \hat{a} gives

$$\hat{I}\hat{a}\hat{I} = \frac{\alpha}{2}(\eta + \eta^{-1})\hat{Z} + i\frac{\alpha}{2}(\eta - \eta^{-1})\hat{Y}, \quad (4)$$

where $\eta \equiv N_+/N_-$, and \hat{Z}, \hat{Y} are the two Pauli matrices in the computational subspace. For large α , $\eta \rightarrow 1$, which results in $\hat{I}\hat{a}\hat{I} = \alpha\hat{Z}$, and we thus see that a single-photon loss event corresponds to a phase-error on the computational basis states. We will refer to the encoding in Eq. (3) as the cat qubit. The computational basis states are shown on the Bloch sphere in [FIG. 1](#).

In order to run QAOA, one needs to prepare all resonators in state $|+\rangle$, i.e., in the case of the cat qubit, the cat state $|C_\alpha^+\rangle$. Such a cat state can be generated deterministically in KNRs by starting from the vacuum, which is an eigenstate of Hamiltonian Eq. (2) for $G = 0$, and then adiabatically increasing G [43, 46]. Since the Hamiltonian in Eq. (2) is symmetric under parity inversion $\hat{a} \rightarrow -\hat{a}$, the KNR follows the adiabatic evolution from the vacuum while also conserving the parity, $[\hat{\Pi}, \hat{H}] = 0$, thus ending up in the even parity cat state $|C_\alpha^+\rangle$. Alternatively, a cat state can also be generated using a sequence of SNAP and displacement gates applied to the vacuum state [47].

B. Set of universal gates on the cat qubit

We are now interested in the implementation of gates on the cat qubit. We are going to focus on the following

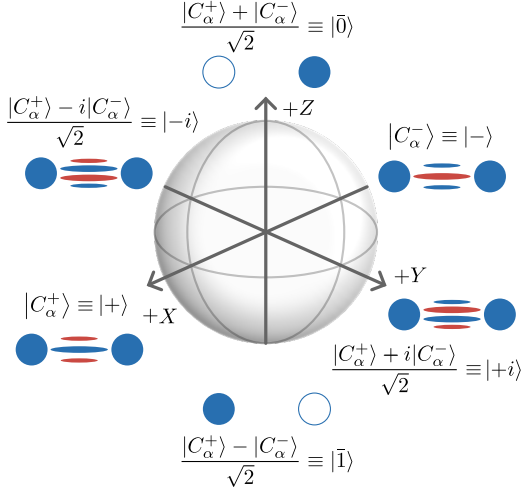


FIG. 1. The computational states that lie along the x, y, z -axis implemented with cat qubits and visualized on the Bloch sphere along with their Wigner function.

gate set:

$$R_Z(\phi) = e^{-i\phi\hat{Z}/2}, \quad (5)$$

$$R_X(\theta) = e^{-i\theta\hat{X}/2}, \quad (6)$$

$$R_Y(\varphi) = e^{-i\varphi\hat{Y}/2}, \quad (7)$$

$$R_{ZZ}(\Theta) = e^{-i\Theta\hat{Z}_1\hat{Z}_2/2}, \quad (8)$$

where $\{\hat{X}, \hat{Y}, \hat{Z}\}$ are the Pauli matrices in the computational basis, which in this case is taken to be the cat qubit Eq. (3). Note that this is an over-complete gate set, as any pair of single-qubit gates $\{R_X(\theta), R_Y(\varphi), R_Z(\phi)\}$ together with $R_{ZZ}(\Theta)$ allow for implementing arbitrary qubit operations. The gates are implemented according to Refs. [42, 43], where the $R_Z(\phi)$ -gate is implemented in KNRs by means of a single-photon drive. The $R_X(\theta)$ -gate is implemented through a time-dependent detuning Δ . The $R_Y(\varphi)$ -gate is implemented by means of single and two-photon drives, and $R_{ZZ}(\Theta)$ -gate is implemented through a beam-splitter interaction between two KNRs. We provide a more detailed description of these gates in Appendix A, where we also present numerical simulations validating this approach for relevant parameter regimes and in presence of noise induced by single-photon loss. In FIG. 2, we plot the average gate fidelity for the $R_Z(\phi)$ -gate as a function of the coherent state amplitudes α , and consider different loss rates to determine the value of α that yields the highest average gate fidelity. In TABLE I we report the average gate fidelities, both without single-photon loss and with a single-photon loss rate of $K/1500$, specifically for the α that yields the optimal gate fidelity in that case, $\alpha = 1.36$. As a consequence of the noise bias and shorter gate-time, we observe that for the cat qubits, the two-qubit R_{ZZ} gate exhibits a higher average gate fidelity compared to the single-qubit R_X and R_Y

gates. However, when comparing the noise-bias preserving single-qubit R_Z gate to the two-qubit R_{ZZ} gate, the single-qubit R_Z gate demonstrates a higher average gate fidelity, as expected.

TABLE I. Average gate fidelities for the considered gates within KNR-encoding obtained through master equation simulation. The results are averaged over 20 points evenly spaced between 0 and π . We consider a single-photon loss rate of $K/1500$ and the corresponding optimal coherent state amplitude $\alpha = 1.36$.

| Gate | Avg. gate fid. (%) with no loss | Avg. gate fid. (%) with single-photon loss |
|------------------|------------------------------------|---|
| $R_Z(\phi)$ | > 99.99 | 99.64 |
| $R_X(\theta)$ | > 99.99 | 98.59 |
| $R_Y(\varphi)$ | 99.52 | 98.72 |
| $R_{ZZ}(\Theta)$ | > 99.99 | 99.15 |

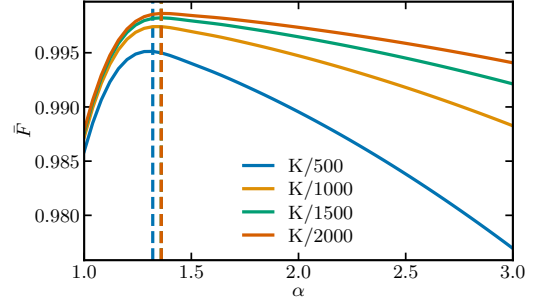


FIG. 2. Average gate fidelity of the $R_Z(\phi)$ -gate as a function of the coherent state amplitude $\alpha = \sqrt{G/K}$, for various single-photon loss rates. The optimal α that results in the maximum average gate fidelity for each loss rate is highlighted with a dashed vertical line. For loss rates varying from $K/1000$ to $K/2000$, the optimal α that achieves the highest average gate fidelity is $\alpha = 1.36$. Conversely, for a loss rate of $K/500$, the ideal α is 1.32.

III. QAOA WITH CAT QUBITS

In this section, we use the gate set defined in Section II B to implement the QAOA sequence on cat qubits. We start by briefly reviewing QAOA, and we then address numerical simulations of increasing complexity (two to eight qubits) in the presence of single-photon losses, assessing the algorithmic performance in terms of the success probability and the approximation ratio.

A. The QAOA algorithm

QAOA [4] starts from the superposition of all possible computational basis states, $|+\rangle^{\otimes n}$, where n is the number of qubits. Then the alternating sequence of the two

parametrized non-commuting quantum gates $\hat{U}(\gamma)$ and $\hat{V}(\beta)$ is applied p times, with

$$\hat{U}(\gamma) \equiv e^{-i\gamma\hat{H}_C}, \quad \hat{V}(\beta) \equiv e^{-i\beta\hat{H}_M}, \quad (9)$$

where $\hat{H}_M \equiv \sum_{i=1}^n \hat{X}_i$ is the mixing Hamiltonian, and \hat{H}_C is the cost Hamiltonian that encodes the solution to the considered optimization problem in its ground state,

$$\hat{H}_C = \sum_{i<j} J_{ij} \hat{Z}_i \hat{Z}_j + \sum_i h_i \hat{Z}_i. \quad (10)$$

Indicating the collection of variational parameters as $\vec{\gamma} = (\gamma_1, \dots, \gamma_p)$ with $\gamma_i \in [0, 2\pi)$ if \hat{H}_C has integer-valued eigenvalues, and $\vec{\beta} = (\beta_1, \dots, \beta_p)$ with $\beta_i \in [0, \pi)$, the final variational state is

$$|\psi_p(\vec{\gamma}, \vec{\beta})\rangle \equiv \hat{V}(\beta_p) \hat{U}(\gamma_p) \dots \hat{V}(\beta_1) \hat{U}(\gamma_1) |+\rangle^{\otimes n}. \quad (11)$$

The parametrized quantum gates are then optimized in a closed loop using a classical optimizer with the objective of minimizing the expectation value of the cost Hamiltonian

$$(\vec{\gamma}^*, \vec{\beta}^*) = \arg \min_{\vec{\gamma}, \vec{\beta}} \langle \psi_p(\vec{\gamma}, \vec{\beta}) | \hat{H}_C | \psi_p(\vec{\gamma}, \vec{\beta}) \rangle. \quad (12)$$

Once the optimal variational parameters are found, one samples from the state $|\psi_p(\vec{\gamma}^*, \vec{\beta}^*)\rangle$ by measuring it in the computational basis, the eigenvalue of the cost Hamiltonian Eq. (10) corresponding to the measured configuration, is evaluated. The success probability is defined as the probability of finding the qubits in the ground state configuration when performing a single shot measurement of the $|\psi_p(\vec{\gamma}, \vec{\beta})\rangle$ state, i.e.

$$F_p(\vec{\gamma}, \vec{\beta}) \equiv \sum_{z_i \in \vec{z}_{\text{sol}}} |\langle z_i | \psi_p(\vec{\gamma}, \vec{\beta}) \rangle|^2, \quad (13)$$

where z_i is a bit-string of length n , and \vec{z}_{sol} is the set of all bit string solutions.

It is clear that QAOA can be run on cat qubits and compiled using the gates discussed in Section II B. The unitary $e^{-i\beta\hat{H}_M}$ can easily be implemented as single qubit $R_X(2\beta)$ -gates on each individual qubit, and the cost Hamiltonian \hat{H}_C can be implemented as a product of $R_Z(2\gamma h_i)$ -gates and $R_{ZZ}(2\gamma J_{ij})$ -gates [48].

B. Solving a toy problem with QAOA on cat qubits

In order to test the capability of cat qubits for solving combinatorial optimization problems using QAOA given relevant gate fidelities for the set of operations considered, we run a master equation simulation of a two-qubit Exact Cover problem on cat qubits.

Exact Cover is an NP-complete problem [49, 50] that appears in logistics, and notably as a part of the Tail Assignment problem [7]. The Exact Cover is formulated

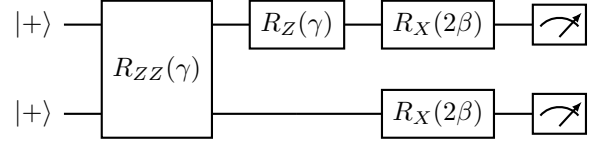


FIG. 3. The circuit diagram of QAOA with depth $p = 1$ for solving a two-qubit instance of the Exact Cover problem, using the universal gate set introduced in Eq. (5)-(8). Here, the circuit is shown using the \hat{X} -mixer.

as follows: given a set $U = \{c_1, c_2, \dots, c_n\}$, and a set of subsets $V = \{V_1, \dots, V_m\}$ with $V_i \subset U$ such that

$$U = \bigcup_{i=1}^m V_i, \quad (14)$$

the goal is to decide if there exists a subset of the set of sets $\{V_i\}$, called R , such that the elements of R are disjoint sets, i.e., $V_i \cap V_j = \emptyset$ for $i \neq j$, and the union of elements of R is U .

For two qubits, the simulation of the circuit with the action of the gates can be carried out by solving the Lindblad master equation for the Kerr resonators. Therefore, we start by simulating Exact Cover for the same toy instance that was considered in Ref. [12], i.e. $U = \{c_1, c_2\}$ and $V = \{V_1, V_2\}$, with $V_1 = \{c_1, c_2\}$ and $V_2 = \{c_2\}$. This has solution $|10\rangle$, corresponding to choosing subset V_1 . The mapping onto the cost Hamiltonian Eq. (10) gives us the values $h_1 = 1/2$, $h_2 = 0$ and $J_{12} = 1/2$ [7]. Therefore, the quantum circuit for implementing QAOA with $p = 1$ takes the form of the one in FIG. 3. We extend our analysis of the original QAOA proposal and allow for different input states, namely $|+\rangle$ and $|+i\rangle$, and mixing Hamiltonians \hat{H}_M . Specifically we do simulations for both \hat{X} and \hat{Y} -mixer, which corresponds to replacing the $R_X(\theta)$ -gate with a $R_Y(\theta)$ -gate in FIG. 3. For simplicity, in the simulation contained in this self-contained sub-section, dealing anyway with a small-size toy model, we chose a non-optimal coherent state amplitude of $\alpha = 2$. FIG. 4 illustrates the amplitude of the pulse schedule for $p = 1$ with the \hat{X} and \hat{Y} mixer respectively for the gates introduced in Section II B. We simulate QAOA implemented with cat qubits using the numerically best found variational parameters $(\vec{\gamma}, \vec{\beta})$ for the ideal, no losses case, up to $p = 2$. The reason for using the variational parameters for the ideal case is that several results have shown that the optimal variational parameters are robust to noise [51, 52], and because it is computational expensive to perform an extensive global optimization simulation of the system.

The results are summarized in TABLE II. First of all, we observe that as a general result (independent of the cat qubit implementation), if the initial state is not an eigenstate of the mixer Hamiltonian, 100% success probability is achieved already for $p = 1$. If, instead, the initial state is an eigenstate of the mixer, $p = 2$ is needed to

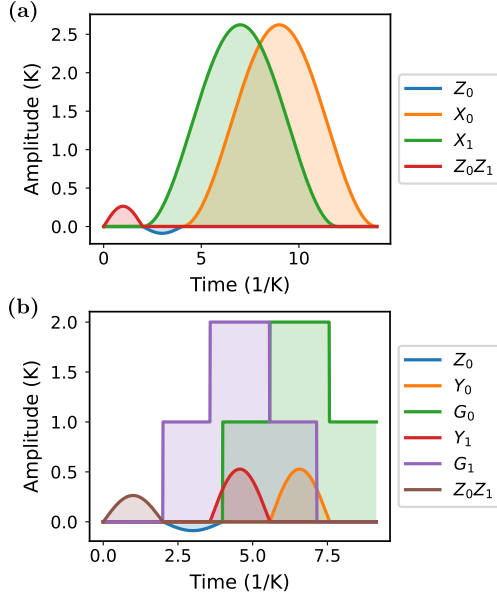


FIG. 4. QAOA depth $p = 1$ pulse schedule and shape (a) with X-mixer, (b) with Y-mixer. Each label corresponds to a Hamiltonian, for example Z_0 corresponds to the amplitude in units of the Kerr non-linearity of the Hamiltonian that implements the R_Z -gate on the zero-th cat qubit. Furthermore, the G -label in (b) corresponds to the amplitude of the two-photon drive, where the unit amplitude corresponds to a net two-photon drive of zero amplitude and the two unit amplitude corresponds to two-photon driving along the P -quadrature. This is because, in the simulations, the two-photon drive is always on. This is not shown in the figure, just as the always present self-Kerr. Therefore, to turn off the always present two-photon drive, an additional two-photon drive Hamiltonian is turned on, but with an opposite amplitude. A more detailed description of how the gates are implemented can be found in Appendix A.

reach 100% success probability. A similar behavior was observed for the MaxCut problem in Ref. [53], where it was shown that designing the mixer Hamiltonian to allow for rotations around the XY -axis leads to a performance increase. In the absence of single-photon losses, these success probabilities are well reproduced when simulating QAOA on cat qubits. Deviations from the ideal case still arise, due to the imperfect average gate fidelities of the gates used to implement the sequence, as per Section II B. In the presence of single-photon losses, the performances of the $R_X(\theta)$ and $R_Y(\theta)$ mixers are almost the same.

C. Numerical results for larger systems: Pauli transfer matrix formalism

We now move forward to more complex simulations. In this section, we numerically simulate solving 6, 8, and 10-qubit MaxCut problems using QAOA with cat qubits and compare it to the case of standard qubits, encoded in

two-level systems, in the presence of single-photon loss for both systems. The MaxCut problem is an NP-complete problem that has been extensively studied in the context of QAOA [11, 54, 55]. The objective of MaxCut is to partition the set of vertices of a graph into two subsets, such that the sum of the edge weights going from one partition to the other is maximum. MaxCut can be formulated as follows: Given a graph $G = (V, E)$, where V is the set of vertices, and E is the set of edges, the MaxCut Hamiltonian is

$$\hat{H}_C = \frac{1}{2} \sum_{i,j \in E} (1 - \hat{Z}_i \hat{Z}_j), \quad (15)$$

where the sum is over all edges.

Since the total Hilbert space dimension increases exponentially with the number of KNRs — The Hilbert space for each KNR is infinite but we truncate it in our numerical simulations to 20 photon levels for each resonator — simulating more than 2 to 3 KNRs quickly becomes computationally difficult. A different strategy is to perform quantum gate set tomography by using the Pauli transfer matrix (PTM) formalism. This technique allows us to map the quantum process of each individual gate to effective two-level systems and, hence, simulate it using the Kraus-operator formalism instead of the Lindblad master equation, which is a lot more computationally efficient.

For a quantum channel $\mathcal{E}(\rho)$ the PTM is formally defined as [56]

$$(R_{\mathcal{E}})_{ij} \equiv \frac{1}{d} \text{Tr} [\hat{P}_i \mathcal{E}(\hat{P}_j)], \quad (16)$$

where $\hat{P}_j \in \{\hat{I}, \hat{X}, \hat{Y}, \hat{Z}\}^{\otimes n}$ is the Pauli group in the computational basis for n -qubits, and $d = 2^n$ is the Hilbert space dimension. Furthermore, the PTM formalism allows for composite maps to be written as a matrix product of the individual PTMs, i.e. $\mathcal{E}_2 \circ \mathcal{E}_1 = R_{\mathcal{E}_2} R_{\mathcal{E}_1}$. Using this fact, we can deconstruct the PTM as a product of two parts: an ideal part R_{ideal} , corresponding to the noiseless ideal gate, and a noise part R_{noise} , corresponding

TABLE II. Performance of QAOA for solving a toy two-qubit instance of Exact Cover on cat qubits for different mixers and initial states. The percentages correspond to the success probability given by Eq. (13), using the optimal angles found numerically. The noisy case corresponds to a single-photon loss rate of $K/1500$. The simulation results were obtained by solving the Schrödinger equation for the ideal case with no losses, and the Lindblad master equation for the noisy case.

| p | Input | Mixer | Ideal QAOA (%) | Cat qb. with no losses (%) | Cat qb. with losses (%) |
|-----|--------------|-------|----------------|----------------------------|-------------------------|
| 1 | $ +\rangle$ | X | 50 | 50.0 | 49.0 |
| 2 | $ +\rangle$ | X | 100 | 99.9 | 90.6 |
| 1 | $ +i\rangle$ | X | 100 | 99.9 | 96.4 |
| 1 | $ +i\rangle$ | Y | 50 | 49.9 | 48.4 |
| 2 | $ +i\rangle$ | Y | 100 | 99.9 | 91.3 |
| 1 | $ +\rangle$ | Y | 100 | 99.9 | 95.8 |

TABLE III. Error channel of the cat qubit for the $R_Z(\pi/2)$, $R_X(\pi/2)$, and $R_{ZZ}(\pi/2)$ -gate. The error channel is shown for coefficients greater than $\geq 10^{-3}$.

| Gate | Error Channel | Coefficients |
|-----------------|---|--|
| $R_Z(\pi/2)$ | $(1 - p)\rho + pZ\rho Z$ | $p = 0.006$ |
| $R_X(\pi/2)$ | $(1 - p_Y - p_Z)\rho + p_Z Z\rho Z + p_Y Y\rho Y + p_Y Z Y\rho Z + p_Z Y Z\rho Y$ | $p_Y = 0.01, p_Z = 0.01, p_{YZ} = p_{ZY} = -0.002$ |
| $R_{ZZ}(\pi/2)$ | $(1 - p_1 - p_2)\rho + p_1 Z_1\rho Z_1 + p_2 Z_2\rho Z_2$ | $p_1 = 0.005, p_2 = 0.005$ |

to both coherent errors as a result of imprecise unitary operation, and incoherent errors stemming from single-photon losses. Since the ideal gate operation is known, it is possible to extract the erroneous part from the full quantum process as follows:

$$R_{\mathcal{E}} = R_{\text{noise}} R_{\text{ideal}} \Rightarrow R_{\text{noise}} = R_{\mathcal{E}} R_{\text{ideal}}^{-1}. \quad (17)$$

We now use the aforementioned procedure in order to transform the continuous time evolution of the KNR gates to PTMs. Since the QAOA implementation of MaxCut only requires $R_X(\theta)$ and $R_{ZZ}(\Theta)$ -gates, we will only focus on these two gates, starting with the former. Because the $R_X(\theta)$ -gate is not noise bias preserving, meaning that single-photon losses do not commute through the gate, the noise part R_{noise} will ultimately depend on the angle θ . We therefore compute R_{noise} for 180 evenly spaced points between 0 and π for the $R_X(\theta)$ -gate, and use the closest R_{noise} for a given θ in upcoming simulations. Hence, we do not need to compute $R_{\mathcal{E}}$ for every possible angle. For the $R_{ZZ}(\Theta)$ -gate, however, we only compute the PTM for $\Theta = 0$, since this gate is noise bias preserving. That is, a single-photon loss corresponds to a \hat{Z} error in the computational subspace, and R_{noise} is thus independent on the angle Θ . For the MaxCut problem, the $R_Z(\phi)$ -gate is not needed for the circuit compilation, and we therefore exclude it.

Once the PTMs have been obtained, we transform them to Kraus operators in order to easily simulate the circuit using Cirq [57] as

$$\hat{\rho} \rightarrow \sum_{k=1}^m \hat{A}_k (\hat{U} \hat{\rho} \hat{U}^\dagger) \hat{A}_k^\dagger, \quad (18)$$

where \hat{U} corresponds to the ideal gate and \hat{A}_k is the set of Kraus operators that describes the noise. Transforming the PTM to Kraus operators can be done by first transforming the PTM to the Choi representation and then transform the Choi-representation to the Kraus representation. To begin, the PTM for a n -qubit channel can be transformed to a Choi-matrix according to [56]

$$\hat{\rho}_{\mathcal{E}} = \frac{1}{d^2} \sum_{i,j=1}^{d^2} (R_{\mathcal{E}})_{ij} \hat{P}_j^T \otimes \hat{P}_i. \quad (19)$$

Given the Choi-matrix, the Kraus-representation is obtained by first diagonalizing the Choi-matrix, from which

its eigenvalues $\{\lambda_i\}$ and eigenvectors $\{|\hat{A}_i\rangle\rangle\}$ are extracted, where $|\cdot\rangle\rangle$ is a superoperator. The eigenvalues and eigenvectors are then used to construct the Kraus operators as follows [58]:

$$\hat{A}_i = \sqrt{\lambda_i} \text{unvec}(|\hat{A}_i\rangle\rangle), \quad (20)$$

where unvec is the unvectorization operation. In TABLE III, we present the error channels for the cat qubit for the $R_Z(\pi/2)$, $R_X(\pi/2)$, and $R_{ZZ}(\pi/2)$ gates, each expanded in the Pauli basis. The results clearly indicate that the $R_Z(\phi)$ and $R_{ZZ}(\Theta)$ gates preserve noise bias, while the $R_X(\theta)$ gate does not.

In order to make a fair comparison between the performance of the cat qubit and the one of the standard qubit, we chose the relevant parameter such that the average gate fidelities are the same between the two systems. By doing so, we can compare which encoding, continuous versus discrete, is the best for QAOA. For the standard qubit device, we implement the $R_X(\theta)$ -gate by evolving under the Pauli \hat{X} , and the $R_{ZZ}(\Theta)$ -gate by evolving under $\hat{Z}_i \hat{Z}_j$. The gate time T_g is chosen to be the same as was used for the cat qubit device, i.e. $T_g = 10/K$ where K is the Kerr non-linearity for the $R_X(\theta)$ -gate and $T_g = 2/K$ for the $R_{ZZ}(\Theta)$ -gate. We specifically pick the relaxation rates T_1 with the pure dephasing rate T_ϕ set to zero, such that the average gate fidelity corresponds to that of the KNR-gates for $\alpha = 1.36$, which maximizes the average gate fidelity in Fig. 2. To this aim, we use an expression for the first-order reduction in the average gate fidelity due to relaxation rate [59]

$$\bar{F} = 1 - \frac{d}{2(d+1)} T_g n \Gamma_1, \quad (21)$$

where \bar{F} is the average gate-fidelity, $d = 2^n$, and $\Gamma_1 = 1/T_1$ is the relaxation rate where T_1 is the relaxation time which we assume to be the same for all n qubits. The

TABLE IV. Average gate fidelities for the $R_{ZZ}(\Theta)$ and $R_X(\theta)$ -gate for cat qubits with $\alpha = 1.36$ and standard qubits obtained using the Kraus operator formalism. The results are averaged over 20 points evenly spaced between 0 and π .

| Avg. gate fid. (%) | $R_{ZZ}(\Theta)$ | $R_X(\theta)$ |
|--------------------|------------------|---------------|
| Cat qubits | 99.16 | 98.60 |
| Standard qubits | 99.16 | 98.62 |

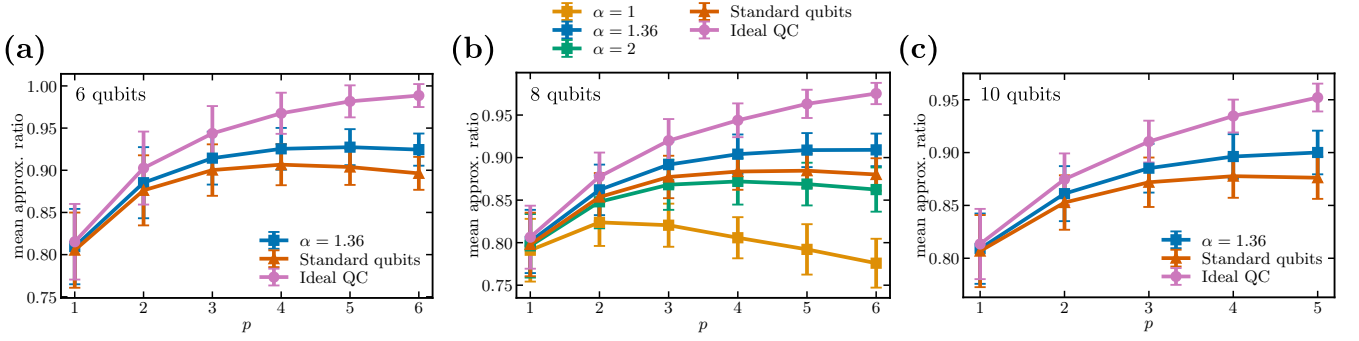


FIG. 5. Mean approximation ratio averaged over 30 instances for MaxCut graphs with 6, 8, and 10 qubits. For the 8-qubit case, we perform additional simulations for three coherent state amplitudes. The circle corresponds to the approximation ratio of an ideal (noise-free) quantum computer. The squares represent the approximation ratio obtained using cat qubits, while the triangles denote the ratio with standard qubits encoded into discrete two-level systems. The average gate fidelity for both cat qubits with amplitude $\alpha = 1.36$ and standard qubits was nearly identical, with values reported in TABLE IV.

expression can be re-written to give the relaxation rate in terms of the average gate-fidelity

$$\Gamma_1 = 2 \frac{(d+1)(1-\bar{F})}{dT_g n}. \quad (22)$$

Using the average gate-fidelities \bar{F} that were numerically calculated for the cat qubits in TABLE I, the corresponding relaxation rates for the standard qubits that results in the same average gate fidelity as for the cat qubits can be obtained.

Likewise, we do quantum gate set tomography using the PTM formalism for the standard qubit device, revealing a less structured error channel as compared as the cat qubit case. Since neither the $R_X(\theta)$ nor the $R_{ZZ}(\Theta)$ -gate are noise bias preserving in this case, we compute R_{noise} for 180 evenly spaced points of θ and Θ between 0 and π for each of the two gates respectively. In TABLE IV we report the average gate fidelity for the $R_{ZZ}(\Theta)$ and $R_X(\theta)$ -gate using the Kraus operator formalism for both cat qubits and the standard qubits after setting the relaxation time T_1 found for the standard qubits. From TABLE IV the average gate fidelities match very well between the cat and standard qubits, with the $R_X(\theta)$ -gate being 0.02% higher for the standard qubits, which we attribute to the fact that Eq. (21) is only a first-order approximation of the average gate fidelity.

Using the Kraus-operator formalism, we are able to simulate QAOA with cat qubits and standard qubits for solving 30 randomly generated 6, 8 and 10-qubit instances of MaxCut on Erdős-Rényi graphs with edge probability $p = 0.5$. As a metric for comparison between the performance of cat qubits and standard qubits, we look at the approximation ratio, defined as

$$r \equiv \frac{\text{Tr}(\hat{\rho} \hat{H}_C)}{C_{\max}}, \quad (23)$$

where the numerator is the expected cut value with $\hat{\rho}$ the density matrix output from QAOA, and C_{\max} is the

value of the maximum cut. The simulation results are presented in FIG. 5. For both standard and cat-qubits, the approximation ratio first increases at increasing p , and then starts decreasing when p is sufficiently high so that the noise in the gates for implementing the QAOA sequence makes it less advantageous to use large depth circuits. The results show that given the same average gate fidelities, the approximation ratio obtained for the KNR device is higher than for the standard qubit device for all iteration levels p , thereby indicating an advantage in the use of the former qubit implementation over the latter. The numerical method used to achieve the classical optimization of the various QAOA instances is described in Appendix B, where we also report on the simulation results for the approximation ratios corresponding to the ideal case, the use of cat qubits, and of standard qubits respectively, without averaging over the random instances.

We provide an explanation for the better performance of cat qubits, by looking at how errors are transformed during the $R_X(\theta)$ and $R_{ZZ}(\Theta)$ gates. As discussed, the dominant error mechanism, i.e. single-photon losses, translates into \hat{Z} -errors in the cat qubit. Consider a \hat{Z} error occurring before the $R_X(\theta)$ gate. By commuting this error through the gate, we derive the following:

$$\begin{aligned} R_X(\theta) \hat{Z} &= e^{-i\theta \hat{X}/2} \hat{Z} \\ &= \cos\left(\frac{\theta}{2}\right) \hat{Z} - i \sin\left(\frac{\theta}{2}\right) \hat{X} \hat{Z} \\ &= \hat{Z} R_X(-\theta), \end{aligned} \quad (24)$$

where in the final equality we have used the anti-commutation relation $\hat{X} \hat{Z} = -\hat{Z} \hat{X}$. This shows that a \hat{Z} error effectively introduces an extra π rotation in the $R_X(\theta)$ gate. Conversely, for the $R_{ZZ}(\Theta)$ gate, a \hat{Z} error on either qubit commutes through the gate.

TABLE III highlights the error channel affecting the cat qubit for these two gates, showing that while the $R_{ZZ}(\Theta)$ gate retains its noise channel structure post-gate

(with \hat{Z} errors), the $R_X(\theta)$ gate alters the channel, introducing \hat{Y} components. In other words, the $R_{ZZ}(\Theta)$ gate is noise-bias preserving while $R_X(\theta)$ is not.

Conversely, one can commute the error through the gate, while preserving the structure of the gate. For the example above, this results in:

$$R_X(\theta)\hat{Z} = (\cos(\theta)\hat{Z} - \sin(\theta)\hat{Y})R_X(\theta). \quad (25)$$

This shows that the $R_X(\theta)$ -gate transforms the \hat{Z} error into a combination of \hat{Z} and \hat{Y} errors, and, in other words, it makes the noise channel unbiased, as can be seen from TABLE III.

Moreover, for a typical MaxCut graph of level- p , the number of $R_{ZZ}(\Theta)$ gates corresponds to the graph's edge count, which averaged 14.1 for the 8-qubit instances, while the count of $R_X(\theta)$ gates is equal to the number of vertices or qubits. There are, in other words more, $R_{ZZ}(\Theta)$ gates than $R_X(\Theta)$ gates in a typical QAOA circuit for the Max-cut problems considered. In contrast to cat qubits, standard qubits are susceptible to \hat{Z} , \hat{X} , and \hat{Y} errors, affecting the fidelity of both $R_X(\theta)$ and $R_{ZZ}(\Theta)$ gates.

We note that the approximation ratio for both standard and cat qubits could be further improved by resorting to error mitigation techniques for estimating expectation values. In particular, in the specific case of virtual distillation [60–62], when noise is present during the error mitigation procedure itself, the advantage of using cat qubits is further enhanced over the use of standard, non noise-biased qubits [37]. Finally, one might wonder whether a better performance in terms of the approximation ratio could be obtained by defining a genuinely bosonic variant of the QAOA algorithm, i.e. by Trotterizing an appropriate bosonic quantum annealing Hamiltonian [38], which initial optimal eigenstate is the vacuum, and which final optimal eigenstate encodes the solution. We explore this question in Appendix C, where we compare the needed mixing and cost Hamiltonian to the case of standard QAOA implemented with cat qubits. Our numerical simulations suggest that such a bosonic QAOA algorithm does not yield an improvement over QAOA on cat qubits. We hypothesize that this missed efficiency stems from the need for bosonic QAOA to bring the state of the system of resonators into the qubit computational basis.

IV. CONCLUSIONS

In conclusion, we have studied implementations of QAOA with a noise-biased qubit, namely the cat qubit, and we have performed numerical simulations in the case that such a cat qubit is implemented by means of a Kerr nonlinear resonator. Despite the algorithmic sequence requiring non-bias preserving X -rotations, running QAOA on such cat qubits yields a performance advantage with respect to the use of standard qubits in the presence of

noise caused by single-photon losses for the studied problem, MaxCut. We expect these results to not be dependent on the chosen problem, and that other problems than MaxCut would benefit from the same performance separation.

Our results indicate that noise-biased qubits that favor dephasing errors, such as cat qubits, are preferable over standard qubits for the implementation of QAOA on near-term intermediate-scale quantum processors, and provide a concrete estimate of the obtainable approximation ratio for MaxCut, for an implementation based on Kerr resonators with realistic noise parameters.

One challenge that pertains to variational algorithms is the so-called barren plateau problem, which refers to the lack of trainability of the parameters caused by an exponentially flat cost function landscape, see e.g. [63]. However, works that consider suboptimal choices of parameters [64, 65] yield viable solutions to the optimization for sizes of up to about hundred qubits. In particular, Ref. [65] points to the possibility of using linear ramps in combination with QAOA (LR-QAOA), where the parameters are not globally optimised, but instead, linear interpolation is considered. An interesting direction would be to tackle larger system sizes, which would require deeper circuits, where making use of these strategies might be helpful.

A further interesting question that stems from our work is if the results here presented, and in particular the performance of QAOA with cat qubits, would further improve in the case where one would adopt a similar encoding of cat qubits in Kerr resonators, but with a more sophisticated use of the detuning as was introduced in Ref. [66], or with the dissipative cat qubits and corresponding gates considered in Ref. [67]. We leave this analysis for future work.

After the online submission of our work as an arXiv preprint we came across an independent work on QAOA with cat qubits [68].

ACKNOWLEDGMENTS

We acknowledge useful discussions with Simone Gasparinetti and Timo Hillmann, as well as Laurent Prost for having suggested us to optimise the amplitude of the coherent states. G. F. acknowledges support from the Vetenskapsrådet (Swedish Research Council) Grant QuACVA. G. F., L. G.-Á., and P. V. acknowledge support from the Knut and Alice Wallenberg Foundation through the Wallenberg Center for Quantum Technology (WACQT). S. P. was supported by the Air Force Office of Scientific Research under award number FA9550-21-1-0209.

CODE AVAILABILITY

The code used for producing the results is made available in Ref. [69]. All master equation simulations are performed using QuTip [70–72].

Appendix A: Quantum gates on cat qubits

In this Appendix, we will go through the implementation of a universal gate set for the cat qubits implemented in a Kerr nonlinear resonator. All gates will be evaluated in terms of their average gate fidelity. The average gate fidelity of a quantum channel \mathcal{E} for a qudit of dimension d is defined as [73]

$$\bar{F}(\mathcal{E}, \hat{U}) = \frac{\sum_j \text{Tr}(\hat{U} \hat{P}_j^\dagger \hat{U}^\dagger \mathcal{E}(\hat{P}_j)) + d^2}{d^2(d+1)}, \quad (\text{A1})$$

where \hat{U} is the target gate and the sum is over the basis of unitary operators \hat{P}_j for the qudit, with \hat{P}_j satisfying $\text{Tr}(\hat{P}_j^\dagger \hat{P}_k) = \delta_{jk}d$. In the simulations we set $d = 2$ for single-qubit gates and $d = 4$ for two-qubit gates, and \hat{P}_j is chosen to be one of the Pauli matrices in the computational basis, e.g. $\hat{P}_j \in \{\hat{I}, \hat{X}, \hat{Y}, \hat{Z}\}^{\otimes n}$, where n is the number of cat qubits. Moreover, in all subsequent simulations we set $\alpha = 1.36$, which corresponds the coherent state amplitude with the highest gate fidelity.

1. $R_Z(\phi)$ -gate

The $R_Z(\phi)$ gate can be performed by applying a single-photon drive with an amplitude of $E(t)$ to the KNR. The Hamiltonian for this drive is given by:

$$\hat{H}_Z(t) = E(t)(\hat{a}e^{-i\theta} + \hat{a}^\dagger e^{i\theta}), \quad (\text{A2})$$

where θ is the phase of the drive. When $\theta = 0$, and $|E(t)| \ll 4G$ and the variation of $E(t)$ is sufficiently slow, the cat qubit is approximately kept in the computational basis [42, 74]. Applying the projector onto the computational subspace $\hat{I} = |\bar{0}\rangle\langle\bar{0}| + |\bar{1}\rangle\langle\bar{1}|$ to the single-photon drive Hamiltonian Eq. (A2) gives for large α

$$\hat{I}E(t)(\hat{a}^\dagger + \hat{a})\hat{I} = 2E(t)\alpha\hat{Z}. \quad (\text{A3})$$

We perform numerical simulations where we set $\Delta = 0$ and define $E(t)$ as

$$E(t) = \frac{\pi\phi}{8T_g\alpha} \sin \frac{\pi t}{T_g}, \quad (\text{A4})$$

with $T_g = 2/K$, and ϕ is the angle for the gate. In FIG. 6 the average gate infidelity $(1 - \bar{F})$ as a function of ϕ for the $R_Z(\phi)$ -gate is shown: in (a) without losses, and in (b) with a single-photon loss rate of $K/1500$.

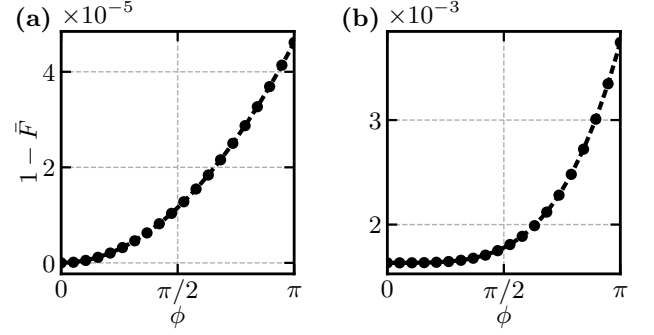


FIG. 6. The average gate infidelity $(1 - \bar{F})$ of the $R_Z(\phi)$ -gate (a) without noise and (b) with a single-photon loss rate of $K/1500$.

2. $R_X(\theta)$ -gate

An $R_X(\theta)$ -gate can be realized by means of a small non-zero detuning Δ between the two-photon drive and the resonator. This can be understood by projecting the number operator in the computational basis:

$$\hat{I}\hat{a}^\dagger\hat{a}\hat{I} = |\alpha|^2\hat{I} - |\alpha|^2e^{-2|\alpha|^2}\hat{X}.$$

If $\Delta(t) \ll 2G$ the computational states $|\bar{0}\rangle$ and $|\bar{1}\rangle$ are approximately kept in the computational subspace. Thus choosing $\Delta(t)$ as

$$\Delta(t) = \frac{\theta\pi}{4T_g|\alpha|^2e^{-2|\alpha|^2}} \sin \frac{\pi t}{T_g} \quad (\text{A5})$$

yields

$$e^{-i[\hat{a}^\dagger\hat{a}\int_0^{T_g}\Delta(t)dt]} = e^{-i\frac{\theta}{2}\hat{X}}, \quad (\text{A6})$$

corresponding to a $R_X(\theta)$ -gate. The disadvantage of this approach, however, is that the gate time T_g has to be exponentially large with respect to α in order to satisfy the condition $\Delta(t) \ll 2G$. For example, if $\alpha = 2$, then a total gate time $T_g > 1000/K$ is required. However, a second proposal was put forward by Goto [42], where the detuning is set to a fixed value Δ_0 , and the corresponding θ that maximizes the average gate fidelity is evaluated. Hence, to perform the $R_X(\theta)$ -gate, $\Delta(t)$ is set to

$$\Delta(t) = \Delta_0 \sin^2 \frac{\pi t}{T_g}, \quad (\text{A7})$$

with $T_g = 10/K$. Throughout this paper, we use this second method. We find the θ that maximizes the average gate fidelity for 20 values of Δ_0 between 0 and $3.95K$, see FIG. 7a. It can be seen that while Δ_0 changes from 0 to $3.95K$, the rotation angle θ changes from 0 to π . In FIG. 7 (b) and (c) the average gate infidelity $(1 - \bar{F})$ as a function of θ for the $R_X(\theta)$ -gate is shown: in (b) without losses, and in (c) with a single-photon loss rate of $K/1500$.

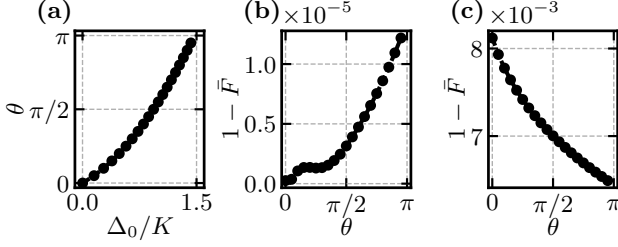


FIG. 7. (a) θ maximizing the average gate fidelity $1 - \bar{F}$ as a function of Δ_0 . (b) Average gate infidelity without noise and (c) with single-photon loss rate of $K/1500$.

3. $R_Y(\varphi)$ -gate

To perform the $R_Y(\varphi)$ -gate, the two-photon drive is turned off for a total time $t = \pi/2K$ to let the state evolve freely under the Kerr Hamiltonian. If the initial state is the vacuum state $|0\rangle_{\text{vac}}$, it will evolve into $(|C_{i\alpha}^+\rangle + i|C_{-i\alpha}^-\rangle)/\sqrt{2}$. Once the state is along the imaginary axis, the two-photon drive is turned on, with a $\pi/2$ phase, so that the state is stabilized along the imaginary axis. Applying the single-photon drive also with a $\pi/2$ phase, such that $\hat{H}_Z(t) = E(t)(\hat{a}^\dagger e^{i\pi/2} + \hat{a}e^{-i\pi/2})$, where $E(t)$ is given by Eq. (A4), the two cat states will acquire a phase difference. When the two-photon drive is turned off for a second time, that is $t = \pi/2K$, the resulting gate is $R_Y(\varphi)$, see FIG. 8. In FIG. 9 the average gate infidelity $(1 - \bar{F})$ as a function of φ for the $R_Y(\varphi)$ -gate is shown in (a) without losses, and with a single-photon loss rate of $K/1500$ in (b).

4. $R_{ZZ}(\Theta)$ -gate

The two-qubit Ising-zz gate $R_{ZZ}(\Theta)$ is achieved by means of two-photon exchange between two KNRs, yielding the coupling Hamiltonian

$$\hat{H}_{ZZ} = g(t)(\hat{a}_1\hat{a}_2^\dagger + \hat{a}_1^\dagger\hat{a}_2). \quad (\text{A8})$$

When $|g(t)| \ll 2G$, the KNRs are approximately kept in the subspace spanned by $|\bar{0}\bar{0}\rangle$, $|\bar{0}\bar{1}\rangle$, $|\bar{1}\bar{0}\rangle$ and $|\bar{1}\bar{1}\rangle$. Projection of Eq. (A8) onto the computational basis yields for large α

$$\hat{H}_{ZZ} = 2\alpha^2 g(t) \hat{Z}_1 \hat{Z}_2 + \text{const.} \quad (\text{A9})$$

In our numerical simulation we set $T_g = 2/K$, and to perform $R_{ZZ}(\Theta)$, we set $g(t)$ as

$$g(t) = \frac{\pi\Theta}{8T_g\alpha^2} \sin \frac{\pi t}{T_g}. \quad (\text{A10})$$

In FIG. 10 the average gate infidelity $(1 - \bar{F})$ as a function of Θ for the $R_{ZZ}(\Theta)$ -gate is shown: in (a) without losses, and in (b) with a single-photon loss rate of $K/1500$.

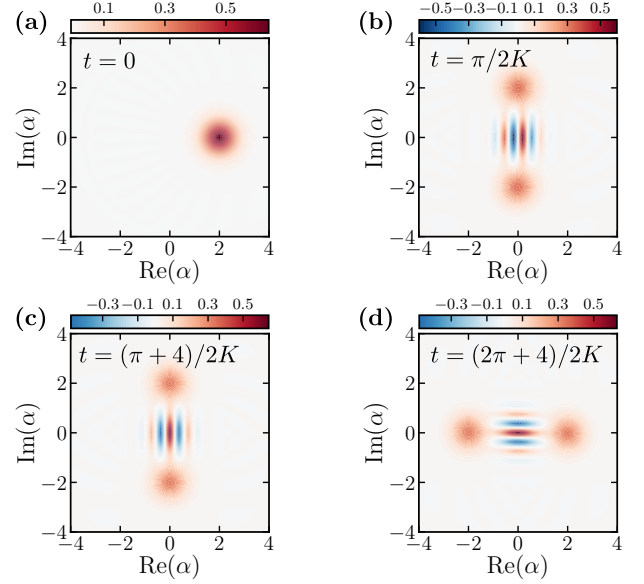


FIG. 8. (a)-(d) Wigner function at four different stages of the $R_Y(\pi/2)$ -gate starting from the $|\bar{0}\rangle$ state. Between (a)-(b) the two-photon drive is turned off to let the state evolve freely under the Kerr Hamiltonian. When a time $t = \pi/2K$ has passed, the two-photon drive is turned on again but this time with a $\pi/2$ phase such that the state is stabilized along the imaginary axis in the phase space. Between (b)-(c), a single-photon drive with a $\pi/2$ is applied to the cat-state for a time $t = 2\pi/K$. This makes the superposition of the two coherent states acquire a phase difference depending on the angle φ . Finally, between (c)-(d), the two-photon drive is turned off once more for a time $t = \pi/2K$ to let the state evolve back and be stabilized along the real axis.

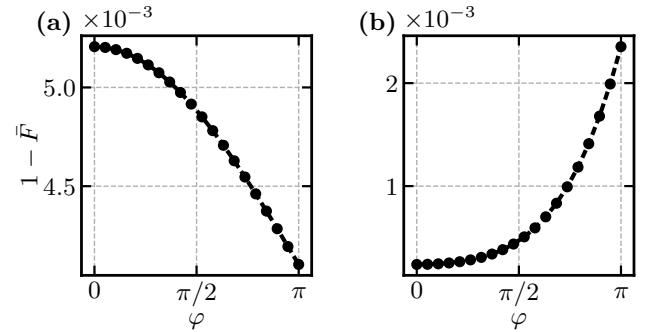


FIG. 9. The average gate infidelity $1 - \bar{F}$ of the $R_Y(\varphi)$ -gate (a) without noise and (b) with single-photon loss rate of $K/1500$.

Appendix B: Numerical optimization and approximation ratios

In this section we elaborate on the classical optimization part of QAOA that was used in Section III C. For $p = 1$, brute force optimization is used where the cost function $\langle \psi_1(\gamma, \beta) | \hat{H}_C | \psi_1(\gamma, \beta) \rangle$ is evaluated on a 100×100

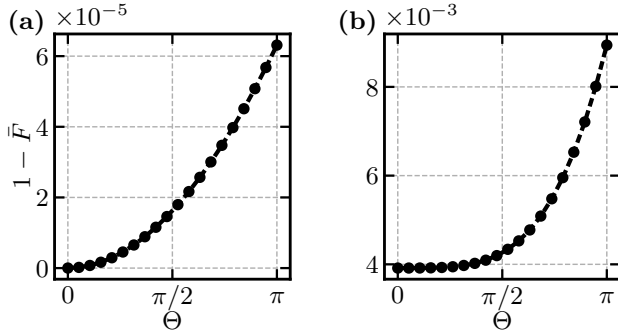


FIG. 10. The average gate infidelity $1 - \bar{F}$ of the $R_{ZZ}(\Theta)$ -gate (a) without noise and (b) with single-photon loss rate of $K/1500$.

grid. For $p > 1$, we use the interpolation method, described in Ref. [75], together with a local optimizer. This strategy consists in predicting a good starting point for the variational parameters search at level $p + 1$ for each individual instance based on the best variational parameters found at level p for the same instance. From the produced starting point, we run a L-BFGS optimizer. FIG. 11 shows the approximation ratio for each instance for noiseless, ideal QAOA as a function of the level p . As can be seen from the figure, the approximation ratio increases at increasing QAOA level for each individual instance, indicating the success of the classical optimizer at finding good variational parameters.

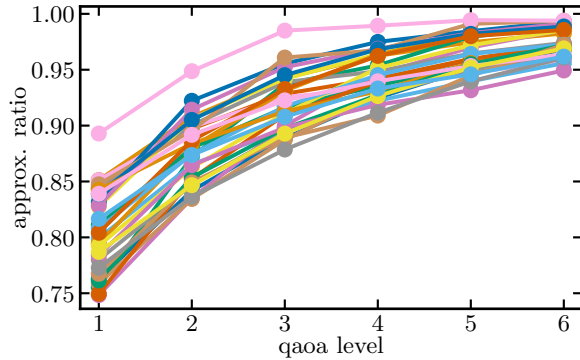


FIG. 11. The approximation ratio as a function of the QAOA level p plotted for each individual instance in the ideal case, meaning no noise. There are 30 instances in total.

Appendix C: Bosonic QAOA

In this Appendix we explore the possibility of deriving a genuinely bosonic version of the QAOA algorithm from Trotterizing a bosonic quantum annealing Hamiltonian, in analogy to what was initially done for qubit QAOA in Ref. [4]. We refer to this new algorithm as

Bosonic QAOA. We compare numerically its performance to QAOA on cat qubits, for the simple case of finding the ground state of a single Ising spin. In this Appendix we chose a coherent state amplitude of $\alpha = 2$ [43].

1. Trotterization of the CV Quantum Annealing Hamiltonian

The time evolution of the quantum annealing algorithm starts from the ground state of a Hamiltonian that is easy to prepare and slowly evolves the system into the ground state of a Hamiltonian encoding the solution to a combinatorial optimization problem. If the evolution is slow enough, as set by the quantum adiabatic theorem, the initial state will follow the instantaneous ground state throughout the evolution and end up in the solution state. The algorithm also works if the initial state is the highest energy eigenstate, or “roof” state, of the initial Hamiltonian, provided the final Hamiltonian encodes the solution in its highest energy eigenstate.

The starting point for deriving a bosonic QAOA algorithm is the quantum annealing Hamiltonian

$$\hat{H}(t) = \left(1 - \frac{t}{\tau}\right) \hat{H}_M + \frac{t}{\tau} \hat{H}_C, \quad (\text{C1})$$

where \hat{H}_M is the initial Hamiltonian, whose ground state is easy to prepare, and \hat{H}_C is the final Hamiltonian, whose ground state encodes the solution to an optimization problem. We take inspiration from the annealing protocol using Kerr resonators of Ref. [38]. For n resonators, we can choose

$$\hat{H}_M = \sum_{i=1}^n (-\Delta \hat{a}_i^\dagger \hat{a}_i - K \hat{a}_i^{\dagger 2} \hat{a}_i^2), \quad (\text{C2})$$

which has the vacuum state $|0\rangle_{\text{vac}}$ as its “roof state”, and

$$\begin{aligned} \hat{H}_C = & \sum_{i=1}^n \left[-K \hat{a}_i^{\dagger 2} \hat{a}_i^2 + G \left(\hat{a}_i^{\dagger 2} + \hat{a}_i^2 \right) \right. \\ & \left. + E_i \left(\hat{a}_i^\dagger + \hat{a}_i \right) \right] + \sum_{1 \leq i < j \leq n} g_{ij} \left(\hat{a}_i^\dagger \hat{a}_j + \hat{a}_j^\dagger \hat{a}_i \right). \end{aligned} \quad (\text{C3})$$

By starting from the vacuum state and slowly increasing t , the instantaneous eigenstate of the Hamiltonian Eq. (C1) evolves into the highest energy eigenstate of \hat{H}_C which encodes the solution to an optimization problem upon cat qubit encoding [38].

We will now, in the spirit of Farhi et al. [4], Trotterize the bosonic quantum annealing Hamiltonian Eq. (C1) to obtain a genuinely bosonic version of QAOA. The continuous-time evolution governed by the time-

TABLE V. Comparison between bosonic QAOA and QAOA in terms of mixer Hamiltonian, cost Hamiltonian and input state.

| | bosonic QAOA | Standard QAOA |
|-------------|---|---|
| \hat{H}_M | $\sum_{i=1}^n [-\Delta \hat{a}_i^\dagger \hat{a}_i - K \hat{a}_i^{\dagger 2} \hat{a}_i^2]$ | $\sum_{i=1}^n [-\Delta(t) \hat{a}_i^\dagger \hat{a}_i - K \hat{a}_i^{\dagger 2} \hat{a}_i^2 + G(\hat{a}_i^{\dagger 2} + \hat{a}_i^2)]$ |
| \hat{H}_C | $\sum_{i=1}^n [-K \hat{a}_i^{\dagger 2} \hat{a}_i^2 + G(\hat{a}_i^{\dagger 2} + \hat{a}_i^2) + E_i(\hat{a}_i + \hat{a}_i^\dagger)]$ $+ \sum_{1 \leq i < j \leq n} g_{ij}(\hat{a}_i^\dagger \hat{a}_j + \hat{a}_j^\dagger \hat{a}_i)$ | $\sum_{i=1}^n [-K \hat{a}_i^{\dagger 2} \hat{a}_i^2 + G(\hat{a}_i^{\dagger 2} + \hat{a}_i^2) + E_i(t)(\hat{a}_i + \hat{a}_i^\dagger)]$ $+ \sum_{1 \leq i < j \leq n} g_{ij}(t)(\hat{a}_j^\dagger \hat{a}_i + \hat{a}_i^\dagger \hat{a}_j)$ |
| Input | $ 0\rangle_{\text{vac}}$ | $ C_\alpha^+\rangle$ |

dependent Hamiltonian of Eq. (C1) is given by

$$\begin{aligned} \hat{U}(T) &\equiv \mathcal{T} \exp \left[-i \int_0^T \hat{H}(t) dt \right] \\ &\approx \prod_{k=1}^p \exp \left[-i \hat{H}(k\delta t) \delta t \right], \end{aligned} \quad (\text{C4})$$

where $\hat{U}(T)$ is the evolution operator from 0 to T , \mathcal{T} is the time-ordering operator, and p is a large integer so that $\delta t = T/p$ is a small time interval. Since \hat{H}_M and \hat{H}_C are two non-commuting Hamiltonians, one can use the Trotter formula:

$$e^{i(A+B)\delta t} = e^{iA\delta t} e^{iB\delta t} + \mathcal{O}(\delta t^2), \quad (\text{C5})$$

for two non-commuting operators A and B given sufficiently small δt , and apply it to the discretized time evolution operator Eq. (C4), yielding

$$\begin{aligned} \hat{U}(T) &\approx \prod_{k=1}^p \exp \left[-i \left(1 - \frac{k\delta t}{\tau} \right) \hat{H}_M \delta t \right] \\ &\quad \times \exp \left[-i \frac{k\delta t}{\tau} \hat{H}_C \delta t \right]. \end{aligned} \quad (\text{C6})$$

We have so far approximated the continuous-time evolution by a sequential product of discrete time steps. We can now apply the same idea underlying the QAOA algorithm in Ref. [4], which consists in truncating this product to an arbitrary positive integer p and redefining the time dependence in each exponent in terms of variational parameters $(1 - k\delta t/\tau)\delta t \rightarrow \beta_k$ and $(k\delta t/\tau)\delta t \rightarrow \gamma_k$, leading to

$$\hat{U}_p = \prod_{k=1}^p \exp \left[-i\beta_k \hat{H}_M \right] \exp \left[-i\gamma_k \hat{H}_C \right]. \quad (\text{C7})$$

We then define our bosonic QAOA algorithm as the sequence in Eq. (C7), with \hat{H}_M and \hat{H}_C given by Eq. (C2) and (C3) respectively, applied to vacuum state chosen as the initial state.

It is interesting to compare the bosonic QAOA algorithm that we derived to the standard QAOA from Section III, when the latter is implemented on cat qubits.

In TABLE V we compare the mixing Hamiltonian, cost Hamiltonian and initial states of bosonic QAOA and QAOA. Clearly, the cost Hamiltonian encoding the problem solution is the same for the two algorithms. Instead, the two-photon drive is not present in the mixer Hamiltonian for bosonic QAOA. The most notable difference is that while the input state for QAOA on cat qubits is the state $|+\rangle$ in all qubits, corresponding to initializing all qubits into a cat state $|C_\alpha^+\rangle$, the input state for bosonic QAOA is the vacuum state.

2. Finding the ground state of a single Ising spin

To test the performance of bosonic QAOA we consider the simplest problem possible — finding the ground state of a single Ising spin in a magnetic field. The cost Hamiltonian for the single Ising spin in a magnetic field is

$$\hat{H}_C = -K \hat{a}^{\dagger 2} \hat{a}^2 + G(\hat{a}^{\dagger 2} + \hat{a}^2) + E(\hat{a}^\dagger + \hat{a}). \quad (\text{C8})$$

In the simulations we begin from the vacuum and we set $\Delta = K/(|\alpha|^2 e^{-2|\alpha|^2})$ and $E = K/(2\alpha)$. The cost Hamiltonian in the computational basis is $\hat{H}_C = \hat{Z}$, whose ground state is $|\bar{1}\rangle$. From the numerical simulations we obtain a fidelity of 0.52 for $p = 1$ and of 0.785 for $p = 2$. In both cases these results were obtained by evaluation of the expectation value of the cost Hamiltonian on a $(100 \times 100)^p$ -grid.

The low fidelity finds an interpretation in terms of the expectation value landscape for $p = 1$, given in FIG. 12a. We see that the landscape is very heavily oscillating, hindering optimization. This should also be compared with the same expectation value landscape of QAOA for qubits which appears instead dramatically smoother, see FIG. 12b. The fidelity is moreover equal to 1 for the $p = 1$ qubits.

A possible interpretation of this difference in the performance of bosonic QAOA and QAOA resides in the fact that bosonic QAOA starts from the vacuum. Hence, the first iterations of the algorithm are needed just to bring the system onto the qubit computational subspace. In contrast, QAOA implemented with qubits (possibly cat qubits) starts already in the computational subspace. The difficulty of preparing the initial cat state is however

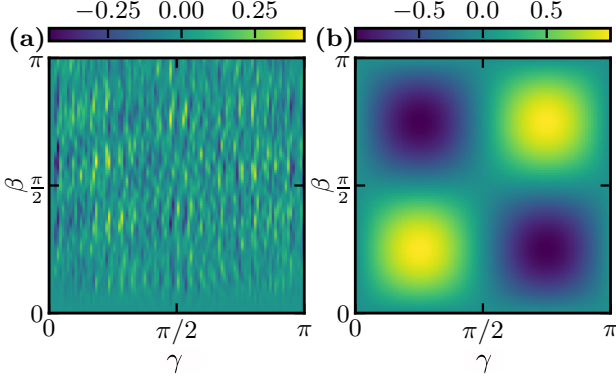


FIG. 12. (a) Expectation value landscape of the single-Ising spin for depth $p = 1$ in bosonic QAOA. (b) Expectation value landscape of the single-Ising spin for $p = 1$ for standard QAOA.

somehow hidden in this comparison. Hence in the next subsection we address the preparation of a cat state with bosonic QAOA.

3. Creating a cat state from vacuum using bosonic QAOA

Here we investigate the possibility of creating a cat state by starting from the vacuum state and by applying bosonic QAOA. The state evolution is

$$\hat{U}_p |0\rangle_{\text{vac}} = \prod_{k=1}^p \exp[-i\beta_k \hat{H}_0] \exp[-i\gamma_k \hat{H}_1] |0\rangle_{\text{vac}} \quad (\text{C9})$$

where the two Hamiltonians are given by

$$\hat{H}_0 = -\Delta \hat{a}^\dagger \hat{a} - K \hat{a}^{\dagger 2} \hat{a}^2, \quad (\text{C10})$$

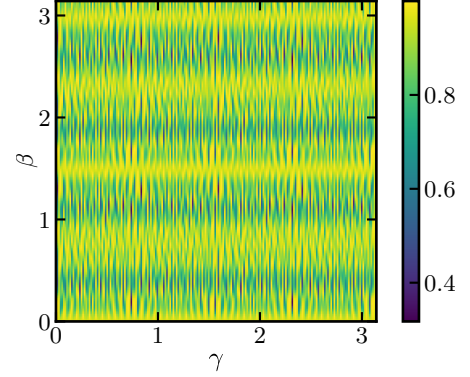


FIG. 13. A section of the $p = 1$ expectation value landscape for generating a target cat-state with bosonic QAOA. The landscape is highly non-convex.

and

$$\hat{H}_1 = -K \hat{a}^{\dagger 2} \hat{a}^2 + G(\hat{a}^{\dagger 2} + \hat{a}^2). \quad (\text{C11})$$

In the simulations, we use $\Delta = K/(|\alpha|^2 e^{-2|\alpha|^2})$ and $G = 4K$, we optimize the angles $(\vec{\gamma}, \vec{\beta})$ numerically with respect to minimizing $F(\alpha, \beta) = 1 - |\langle C_\alpha^+ | \psi_1(\alpha, \beta) \rangle|^2$. FIG. 13 shows $F(\alpha, \beta)$, where it can be seen that the landscape is highly non-convex and finding the global minimum is challenging. As a result, we obtain a poor fidelity of the variational state with the target cat state, $|\langle C_\alpha^+ | \psi_1(\alpha^*, \beta^*) \rangle|^2 = 0.57$.

-
- [1] M. Cerezo, A. Arrasmith, R. Babbush, S. C. Benjamin, S. Endo, K. Fujii, J. R. McClean, K. Mitarai, X. Yuan, L. Cincio, and P. J. Coles, “Variational quantum algorithms”, *Nature Reviews Physics* **3**, 625 (2021).
 - [2] A. Montanaro, “Quantum algorithms: an overview”, *npj Quantum Information* **2**, 15023 (2016).
 - [3] J. Preskill, “Quantum Computing in the NISQ era and beyond”, *Quantum* **2**, 79 (2018).
 - [4] E. Farhi, J. Goldstone, and S. Gutmann, “A Quantum Approximate Optimization Algorithm”, *arXiv:1411.4028 [quant-ph]* (2014).
 - [5] M. Streif, S. Yarkoni, A. Skolik, F. Neukart, and M. Leib, “Beating classical heuristics for the binary paint shop problem with the quantum approximate optimization algorithm”, *Physical Review A* **104**, 012403 (2021).
 - [6] D. Fitzek, T. Ghandriz, L. Laine, M. Granath, and A. F. Kockum, “Applying quantum approximate optimization to the heterogeneous vehicle routing problem”, *arXiv:2110.06799 [quant-ph]* (2021).
 - [7] P. Vikstål, M. Grönkvist, M. Svensson, M. Andersson, G. Johansson, and G. Ferrini, “Applying the Quantum Approximate Optimization Algorithm to the Tail-Assignment Problem”, *Physical Review Applied* **14**, 034009 (2020).
 - [8] T. Stollenwerk, E. Lobe, and M. Jung, in *International Workshop on Quantum Technology and Optimization Problems* (Springer, 2019) pp. 99–110.
 - [9] M. Hodson, B. Ruck, H. Ong, D. Garvin, and S. Dulman, “Portfolio rebalancing experiments using the quantum alternating operator ansatz”, *arXiv:1911.05296 [quant-ph]* (2019).
 - [10] J. S. Otterbach, R. Manenti, N. Alidoust, A. Bestwick, M. Block, B. Bloom, S. Caldwell, N. Didier, E. S. Fried, S. Hong, P. Karalekas, C. B. Osborn, A. Papageorge, E. C. Peterson, G. Prawiroatmodjo, N. Rubin, C. A. Ryan, D. Scarabelli, M. Scheer, E. A. Sete, P. Sivarajah, R. S. Smith, A. Staley, N. Tezak, W. J. Zeng, A. Hudson, B. R. Johnson, M. Reagor, M. P. da Silva, and C. Rigetti, “Unsupervised machine learning on a hybrid quantum computer”, *arxiv:1712.05771 [quant-ph]* (2017).
 - [11] M. P. Harrigan *et al.*, “Quantum approximate optimization of non-planar graph problems on a planar superconducting processor”, *Nature Physics* **17**, 332–336 (2021).

- [12] A. Bengtsson, P. Vikstål, C. Warren, M. Svensson, X. Gu, A. F. Kockum, P. Krantz, C. Križan, D. Shiri, I.-M. Svensson, G. Tancredi, G. Johansson, P. Delsing, G. Ferrini, and J. Bylander, “Improved Success Probability with Greater Circuit Depth for the Quantum Approximate Optimization Algorithm”, *Physical Review Applied* **14**, 034010 (2020).
- [13] N. Lacroix, C. Hellings, C. K. Andersen, A. Di Paolo, A. Remm, S. Lazar, S. Krinner, G. J. Norris, M. Gabureac, J. Heinsoo, A. Blais, C. Eichler, and A. Wallraff, “Improving the performance of deep quantum optimization algorithms with continuous gate sets”, *PRX Quantum* **1**, 110304 (2020).
- [14] O. Pfister, “Continuous-variable quantum computing in the quantum optical frequency comb”, *Journal of Physics B: Atomic, Molecular and Optical Physics* **53**, 012001 (2019).
- [15] A. L. Grimsmo and A. Blais, “Squeezing and quantum state engineering with josephson travelling wave amplifiers”, *npj Quantum Information* **3**, 1–11 (2017).
- [16] T. Hillmann, F. Quijandria, G. Johansson, A. Ferraro, S. Gasparinetti, and G. Ferrini, “Universal Gate Set for Continuous-Variable Quantum Computation with Microwave Circuits”, *Physical Review Letters* **125**, 160501 (2020).
- [17] P. Campagne-Ibarcq, A. Eickbusch, S. Touzard, E. Zalts-Geller, N. E. Frattini, V. V. Sivak, P. Reinhold, S. Puri, S. Shankar, R. J. Schoelkopf, L. Frunzio, M. Mirrahimi, and M. H. Devoret, “Quantum error correction of a qubit encoded in grid states of an oscillator”, *Nature* **584**, 368–372 (2020).
- [18] A. Serafini, A. Retzker, and M. B. Plenio, “Manipulating the quantum information of the radial modes of trapped ions: linear phononics, entanglement generation, quantum state transmission and non-locality tests”, *New Journal of Physics* **11**, 023007 (2009).
- [19] C. Flühmann, T. L. Nguyen, M. Marinelli, V. Negnevitsky, K. Mehta, and J. P. Home, “Encoding a qubit in a trapped-ion mechanical oscillator”, *Nature* **566**, 513–517 (2019).
- [20] B. de Neeve, T.-L. Nguyen, T. Behrle, and J. P. Home, “Error correction of a logical grid state qubit by dissipative pumping”, *Nature Physics* **18**, 296–300 (2022).
- [21] M. Schmidt, M. Ludwig, and F. Marquardt, “Optomechanical circuits for nanomechanical continuous variable quantum state processing”, *New Journal of Physics* **14**, 125005 (2012).
- [22] O. Houhou, H. Aissaoui, and A. Ferraro, “Generation of cluster states in optomechanical quantum systems”, *Physical Review A* **92**, 063843 (2015).
- [23] W. H. P. Nielsen, Y. Tsaturyan, C. B. Møller, E. S. Polzik, and A. Schliesser, “Multimode optomechanical system in the quantum regime”, *Proceedings of the National Academy of Sciences* **114**, 62–66 (2017).
- [24] J. Stasińska, C. Rodó, S. Paganelli, G. Birkel, and A. Sanpera, “Manipulating mesoscopic multipartite entanglement with atom-light interfaces”, *Physical Review A* **80**, 062304 (2009).
- [25] D. F. Milne and N. V. Korolkova, “Composite-cluster states and alternative architectures for one-way quantum computation”, *Physical Review A* **85**, 032310 (2012).
- [26] Y. Ikeda and N. Yamamoto, “Deterministic generation of gaussian pure states in a quasilocal dissipative system”, *Physical Review A* **87**, 033802 (2013).
- [27] K. R. Motes, B. Q. Baragiola, A. Gilchrist, and N. C. Menicucci, “Encoding qubits into oscillators with atomic ensembles and squeezed light”, *Physical Review A* **95**, 053819 (2017).
- [28] L. Aolita, A. J. Roncaglia, A. Ferraro, and A. Acín, “Gapped two-body hamiltonian for continuous-variable quantum computation”, *Physical Review Letters* **106**, 090501 (2011).
- [29] N. Ofek, A. Petrenko, R. Heeres, P. Reinhold, Z. Leghtas, B. Vlastakis, Y. Liu, L. Frunzio, S. M. Girvin, L. Jiang, M. Mirrahimi, M. H. Devoret, and R. J. Schoelkopf, “Extending the lifetime of a quantum bit with error correction in superconducting circuits”, *Nature* **536**, 441–445 (2016).
- [30] Z. Ni, S. Li, X. Deng, Y. Cai, L. Zhang, W. Wang, Z.-B. Yang, H. Yu, F. Yan, S. Liu, C.-L. Zou, L. Sun, S.-B. Zheng, Y. Xu, and D. Yu, “Beating the break-even point with a discrete-variable-encoded logical qubit”, *Nature* **616**, 56–60 (2023).
- [31] V. V. Sivak, A. Eickbusch, B. Royer, S. Singh, I. Tsioutsios, S. Ganjam, A. Miano, B. L. Brock, A. Z. Ding, L. Frunzio, S. M. Girvin, R. J. Schoelkopf, and M. H. Devoret, “Real-time quantum error correction beyond break-even”, *Nature* **616**, 50–55 (2023).
- [32] G. Verdon, J. M. Arrazola, K. Brádler, and N. Killoran, “A quantum approximate optimization algorithm for continuous problems”, *arXiv:1902.00409 [quant-ph]* (2019).
- [33] Y. Enomoto, K. Anai, K. Udagawa, and S. Takeda, “Continuous-variable quantum approximate optimization on a programmable photonic quantum processor”, *Phys. Rev. Res.* **5**, 043005 (2023).
- [34] P. Aliferis and J. Preskill, “Fault-tolerant quantum computation against biased noise”, *Phys. Rev. A* **78**, 052331 (2008).
- [35] D. K. Tuckett, S. D. Bartlett, and S. T. Flammia, “Ultra-high error threshold for surface codes with biased noise”, *Phys. Rev. Lett.* **120**, 050505 (2018).
- [36] E. Gouzien, D. Ruiz, F.-M. Le Régent, J. Guillaud, and N. Sangouard, “Performance analysis of a repetition cat code architecture: Computing 256-bit elliptic curve logarithm in 9 hours with 126 133 cat qubits”, *Phys. Rev. Lett.* **131**, 040602 (2023).
- [37] P. Vikstål, G. Ferrini, and S. Puri, “Study of noise in virtual distillation circuits for quantum error mitigation”, *Quantum* **8**, 1441 (2024).
- [38] S. Puri, C. K. Andersen, A. L. Grimsmo, and A. Blais, “Quantum annealing with all-to-all connected nonlinear oscillators”, *Nature Communications* **8**, 15785 (2017).
- [39] A. Grimm, N. E. Frattini, S. Puri, S. O. Mundhada, S. Touzard, M. Mirrahimi, S. M. Girvin, S. Shankar, and M. H. Devoret, “Stabilization and operation of a kerr-cat qubit”, *Nature* **584**, 205–209 (2020).
- [40] K. Takase, A. Kawasaki, B. K. Jeong, M. Endo, T. Kashiwazaki, T. Kazama, K. Enbutsu, K. Watanabe, T. Umeki, S. Miki, H. Terai, M. Yabuno, F. China, W. Asavanant, J.-i. Yoshikawa, and A. Furusawa, “Generation of schrödinger cat states with wigner negativity using a continuous-wave low-loss waveguide optical parametric amplifier”, *Opt. Express* **30**, 14161 (2022).
- [41] M. Cosacchi, T. Seidelmann, J. Wiercinski, M. Cygorek, A. Vagov, D. E. Reiter, and V. M. Axt, “Schrödinger cat states in quantum-dot-cavity systems”, *Phys. Rev. Research* **3**, 023088 (2021).

- [42] H. Goto, “Universal quantum computation with a nonlinear oscillator network”, *Phys. Rev. A* **93**, 050301(R) (2016).
- [43] S. Puri, S. Boutin, and A. Blais, “Engineering the quantum states of light in a kerr-nonlinear resonator by two-photon driving”, *npj Quantum Inf* **3**, 18 (2017).
- [44] S. Puri, L. St-Jean, J. A. Gross, A. Grimm, N. E. Fratini, P. S. Iyer, A. Krishna, S. Touzard, L. Jiang, A. Blais, S. T. Flammia, and S. M. Girvin, “Bias-preserving gates with stabilized cat qubits”, *Sci Adv* **6**, eaay5901 (2020).
- [45] S. Puri, A. Grimm, P. Campagne-Ibarcq, A. Eickbusch, K. Noh, G. Roberts, L. Jiang, M. Mirrahimi, M. H. Devoret, and S. M. Girvin, “Stabilized cat in driven nonlinear cavity”, *Phys. Rev. X* **9**, 041009 (2019).
- [46] H. Goto, “Bifurcation-based adiabatic quantum computation with a nonlinear oscillator network”, *Sci Rep* **6**, 21686 (2016).
- [47] M. Kudra, M. Kervinen, I. Strandberg, S. Ahmed, M. Scigliuzzo, A. Osman, D. P. Lozano, M. O. Tholén, R. Borgani, D. B. Haviland, G. Ferrini, J. Bylander, A. F. Kockum, F. Quijandria, P. Delsing, and S. Gasparinetti, “Robust preparation of wigner-negative states with optimized snap-displacement sequences”, *PRX Quantum* **3**, 030301 (2022).
- [48] P. Vikstål, *Application of the quantum approximate optimization algorithm to combinatorial optimization problems*, *Licentiate thesis*, Chalmers University of Technology (2020).
- [49] R. M. Karp, in *Complexity of Computer Computations: Proceedings of a symposium on the Complexity of Computer Computations, held March 20–22, 1972, at the IBM Thomas J. Watson Research Center, Yorktown Heights, New York, and sponsored by the Office of Naval Research, Mathematics Program, IBM World Trade Corporation, and the IBM Research Mathematical Sciences Department*, The IBM Research Symposia Series, edited by R. E. Miller, J. W. Thatcher, and J. D. Bohlinger (Springer US, 1972) pp. 85–103.
- [50] M. R. Garey and D. S. Johnson, *Computers and Intractability: A Guide to the Theory of NP-Completeness* (W.H. Freeman and Company, 1979).
- [51] C. Xue, Z.-Y. Chen, Y.-C. Wu, and G.-P. Guo, “Effects of quantum noise on quantum approximate optimization algorithm”, *Chinese Physics Letters* **38**, 030302 (2021).
- [52] K. Sharma, S. Khatri, M. Cerezo, and P. J. Coles, “Noise resilience of variational quantum compiling”, *New J. Phys.* **22**, 043006 (2020).
- [53] L. C. G. Govia, C. Poole, M. Saffman, and H. K. Krovi, “Freedom of the mixer rotation axis improves performance in the quantum approximate optimization algorithm”, *Phys. Rev. A* **104**, 062428 (2021).
- [54] E. Farhi, D. Gamarnik, and S. Gutmann, “The quantum approximate optimization algorithm needs to see the whole graph: Worst case examples”, *arXiv:2005.08747 [quant-ph]* (2020).
- [55] J. Wurtz and P. Love, “MaxCut quantum approximate optimization algorithm performance guarantees for $p > 1$ ”, *Phys. Rev. A* **103**, 042612 (2021).
- [56] D. Greenbaum, “Introduction to quantum gate set tomography”, *arXiv:1509.02921 [quant-ph]* (2015).
- [57] Cirq Developers, “Cirq (v0.12.0)”, Zenodo, <https://doi.org/10.5281/zenodo.5182845> (2021).
- [58] C. J. Wood, J. D. Biamonte, and D. G. Cory, “Tensor networks and graphical calculus for open quantum systems”, *Quantum Info. Comput.* **15**, 759–811 (2015).
- [59] T. Abad, J. Fernández-Pendás, A. Frisk Kockum, and G. Johansson, “Universal fidelity reduction of quantum operations from weak dissipation”, *Phys. Rev. Lett.* **129**, 150504 (2022).
- [60] J. Cotler, S. Choi, A. Lukin, H. Gharibyan, T. Grover, M. E. Tai, M. Rispoli, R. Schittko, P. M. Preiss, A. M. Kaufman, M. Greiner, H. Pichler, and P. Hayden, “Quantum virtual cooling”, *Phys. Rev. X* **9**, 031013 (2019).
- [61] B. Koczor, “Exponential error suppression for near-term quantum devices”, *Phys. Rev. X* **11**, 031057 (2021).
- [62] W. J. Huggins, S. McArdle, T. E. O’Brien, J. Lee, N. C. Rubin, S. Boixo, K. B. Whaley, R. Babbush, and J. R. McClean, “Virtual distillation for quantum error mitigation”, *Phys. Rev. X* **11**, 041036 (2021).
- [63] L. Bittel and M. Kliesch, “Training variational quantum algorithms is np-hard”, *Physical review letters* **127**, 120502 (2021).
- [64] R. Sreedhar, P. Vikstål, M. Svensson, A. Ask, G. Johansson, and L. García-Álvarez, “The quantum approximate optimization algorithm performance with low entanglement and high circuit depth”, *arXiv:2207.03404 [quant-ph]* (2022).
- [65] J. A. Montanez-Barrera and K. Michielsen, “Towards a universal qaoa protocol: Evidence of a scaling advantage in solving some combinatorial optimization problems”, *arXiv:2405.09169 [quant-ph]* (2024).
- [66] D. Ruiz, R. Gautier, J. Guillaud, and M. Mirrahimi, “Two-photon driven kerr quantum oscillator with multiple spectral degeneracies”, *Phys. Rev. A* **107**, 042407 (2023).
- [67] R. Gautier, M. Mirrahimi, and A. Sarlette, “Designing high-fidelity zeno gates for dissipative cat qubits”, *PRX Quantum* **4**, 040316 (2023).
- [68] A.-S. Bornens and M. Nowak, “Variational quantum algorithms on cat qubits”, *arXiv:2305.14143 [quant-ph]* (2023).
- [69] P. Wikstahl, “Wikstahl/qaoa-with-cat-qubits: Release v1.0 (v1.0)”, Zenodo, <https://doi.org/10.5281/zenodo.7915751> (2023).
- [70] J. R. Johansson, P. D. Nation, and F. Nori, “QuTiP: An open-source python framework for the dynamics of open quantum systems”, *Computer Physics Communications* **183**, 1760–1772 (2012).
- [71] J. R. Johansson, P. D. Nation, and F. Nori, “QuTiP 2: A python framework for the dynamics of open quantum systems”, *Computer Physics Communications* **184**, 1234–1240 (2013).
- [72] B. Li, S. Ahmed, S. Saraogi, N. Lambert, F. Nori, A. Pitchford, and N. Shammah, “Pulse-level noisy quantum circuits with QuTiP”, *Quantum* **6**, 630 (2022).
- [73] M. A. Nielsen, “A simple formula for the average gate fidelity of a quantum dynamical operation”, *Physics Letters A* **303**, 249–252 (2002).
- [74] P. Vikstål, *Continuous-variable quantum annealing with superconducting circuits*, *Masters thesis*, Linköping University (2018).
- [75] L. Zhou, S.-T. Wang, S. Choi, H. Pichler, and M. D. Lukin, “Quantum approximate optimization algorithm: Performance, mechanism, and implementation on near-term devices”, *Phys. Rev. X* **10**, 021067 (2020).